

Dynamic rupture modeling on the Hayward Fault, northern California – estimating coseismic and postseismic hazards of partially creeping faults

Julian C. Lozos, California State University, Northridge

Gareth J. Funning, University of California, Riverside

This material is based upon work supported by the U.S. Geological Survey under Grant Nos. G17AP00066 and G17AP00067.

The views and conclusions contained in this document are those of the authors and should not be interpreted as representing the opinions or policies of the U.S. Geological Survey. Mention of trade names or commercial products does not constitute their endorsement by the U.S. Geological Survey.

ABSTRACT

The hazards associated with partially creeping faults – faults that have areas that are undergoing aseismic creep, yet also have areas that are frictionally locked and are subject to damaging earthquakes – are not fully understood. In particular, the degree to which earthquake rupture is able to propagate into creeping areas of the fault, and the amount of shallow accelerated creep that would follow such an earthquake are both uncertain. Here, we explore the controls that frictional conditions, fault geometry, and accumulated elastic stresses have on these processes for the Hayward Fault in the San Francisco Bay Area, California, through a series of dynamic rupture simulations using rate-state friction, integrated with static boundary element interseismic loading and afterslip models.

We find that frictional contrast between creeping and locked fault patches alone is enough to limit rupture extent, as is stress reduction in creeping patches. On the Hayward Fault, the combination of rate-strengthening friction and reduced stress keeps dynamic rupture confined to a central locked patch of the fault. Smaller locked patches may begin to slip, but if they are surrounded by creep, the stress drop there is incomplete and the rupture cannot grow. Parameterizing creeping sections with rate-neutral behavior allows slightly larger ruptures, but the same first-order effects persist. An unreleased slip deficit, which we assume is released as rapid postseismic creep (afterslip), exists on fault sections which did not slip completely or slip at all coseismically, and is at its largest at the edges of the fault, and, in many cases, in a zone surrounding the coseismic rupture zone – particularly in cases in which we parameterize creeping sections with rate-strengthening friction. This afterslip may drive unruptured locked patches of the Hayward Fault to produce significant aftershocks, and may also accelerate loading rates on adjacent faults. It may also pose a hazard in its own right, to fault-crossing infrastructure lifelines.

While this study is focused on the Hayward Fault, our findings should enable more accurate scenario modeling and hazard analysis for earthquakes on other partially creeping faults, including major faults close to large regional populations in California (e.g. the Calaveras, Rodgers Creek and Concord faults).

INTRODUCTION

The hazards associated with partially creeping faults – faults that have areas that are undergoing aseismic creep, yet also have areas that are frictionally locked and are subject to damaging earthquakes – are not fully understood. In particular, the degree to which earthquake rupture is able to propagate into creeping areas of the fault, and the amount of shallow accelerated creep that would follow an earthquake are both uncertain. Both of these questions are gaps in our understanding of the physics of fault slip in general, but they are brought to particular societal relevance by the Hayward Fault, a partially-creeping fault which underlies the densely populated eastern San Francisco Bay Area.

The occurrence of aseismic creep on a fault has a significant effect on the rate of strain accumulation. Since the portions of faults that creep are moving interseismically, rather than remaining locked, they accumulate less elastic strain energy than stick-slip faults. For the most part, the rate of creep is lower than the long-term slip rate of the fault estimated geologically [Lienkaemper *et al.*, 1991; Schmidt *et al.*, 2005; d'Alessio *et al.*, 2005], meaning that even though the fault is not locked, it is still accumulating strain, though at a lower rate than for a fully locked fault. We would therefore expect a lower seismic moment if an earthquake were to occur on such a fault, compared with a fault of the same size that did not creep. In the seismic hazard estimates computed for California, such as the Uniform California Earthquake Hazard Forecast (UCERF), this effect is accounted for in calculations of potential seismic moment by scaling by a coupling coefficient that depends on the ratio of surface creep rate to long-term slip rate [Field *et al.*, 2014].

The friction regime of partially creeping faults may also limit their rupture behaviors. In the nomenclature of rate-state friction [Dieterich, 1978; Ruina, 1983], we would consider stick-slip behavior “velocity-weakening” – movement of the fault weakens the frictional resistance of the fault to movement, causing a positive feedback that promotes rapid, unstable seismic slip. Creep, on the other hand, implies “velocity-strengthening” behavior – frictional strength of the fault increases with fault slip rate, acting to suppress rapid fault slip and promote stable sliding. There is evidence to suggest that regions of faults with contrasting frictional regimes persist throughout the earthquake cycle. This can be seen in geodetic data from multiple earthquake cycles on the Parkfield segment of the San Andreas Fault, where an asperity shown to be responsible for M6 earthquakes in 1934, 1966, and 2004 is surrounded by regions that undergo creep during interseismic periods [Murray and Langbein, 2006]. In the week following the 2004 earthquake, the creeping portions of the fault released their accumulated elastic strain energy through accelerated postseismic creep, also referred to as “shallow afterslip” [Johanson *et al.*, 2006]. The implication here is that creeping fault segments may also act as barriers to earthquake rupture, restricting rupture length, and thus reducing seismic hazard. This effect is implemented in UCERF3 by the inclusion of an “aseismicity factor” related to the area of the fault undergoing aseismic creep, and that therefore will not sustain seismic rupture [Field *et al.*, 2014]; we test this assumption with modeling here.

Regardless of rupture length, the hazards and risks posed by partially creeping faults are twofold. Traditionally, estimates of earthquake risk have focused upon the ‘coseismic hazard’ – the strong shaking that accompanies earthquake rupture, and its secondary effects (e.g. liquefaction, fire-following-earthquake, triggered landsliding). There is no observational difference in ground

acceleration between earthquakes on partially creeping faults and comparably sized events on locked faults [e.g. *Harris and Abrahamson, 2014*]; as such, the expected shaking hazards should be no less severe for partially creeping faults. As such, we choose not to focus on ground motions generated from our model ruptures here.

However, partially creeping faults pose an additional, postseismic, hazard beyond the traditional coseismic hazard. Accelerated postseismic creep that may follow such an event can pose an additional risk, especially to lifelines and structures that span the fault trace and could be further damaged by ongoing fault movement. A prominent example of such a hazard was the large, rapid, shallow afterslip on portions of the West Napa fault following the 2014 South Napa earthquake [e.g. *Lienkaemper et al., 2016; Floyd et al., 2016*]. This accelerated creep was responsible for continued road damage at multiple locations for a few days after the mainshock, and also motivated replacement of a gas pipeline [*Kelson and Westling, 2014*]. In areas close to partially creeping faults it is therefore important to consider both types of hazard in risk assessments and planning of post-event response. For example, in order to avoid postseismic damage to pipes or power lines when effecting repairs in the immediate aftermath of the earthquake, an estimate of the expected total amount of accelerated surface creep would be crucial.

Here, we focus on the Hayward fault in the San Francisco Bay Area, California as our main test case. The most recent major earthquake on the Hayward Fault was a $M \sim 6.8$ event in 1868, which caused significant surface displacement and notable building damage in a 40 km-long zone between the present-day cities of Oakland and Fremont [*Yu and Segall, 1996; Boatwright and Bundock, 2008, Figure 1A*]. In addition, present-day surface creep rates of 3–8 mm/yr are measured geodetically [e.g. *McFarland et al., 2016; Funning et al., 2009*]. We select the Hayward fault for two reasons: First, we can place good constraints on the subsurface geometry and creep distribution on the fault, using a combination of high-precision seismic locations for the former and geodetic data for the latter [e.g. *Waldhauser and Schaff, 2008; Funning et al., 2009; Funning and Bürgmann, 2014*]. Second, the eastern San Francisco Bay Area, the location of the Hayward fault, is home to over two million people, the largest local population threatened by a partially creeping fault, to our knowledge, drawing a sharp focus on the need to accurately quantify the seismic hazard faced.

Aagaard et al. used kinematic [2010a, 2010b] and probabilistic [2012] models to explore the question of rupture across creeping fault sections on the Hayward Fault, but neither of these methods address the physics of how a creeping section may control the length of a rupture. *Lozos et al.* [2015a] used dynamic models to address this question for the partially creeping Bartlett Springs fault but that study used slip-weakening friction, which cannot capture any recovery of frictional strength that may occur during a rupture. Their study also did not directly calculate how interseismic creep influences pre-earthquake stress concentrations. *Harris et al.* [submitted] conducted dynamic rupture models on the connected Rodgers Creek, Hayward, and Calaveras faults, and found that creeping sections can indeed inhibit rupture propagation through this system. This study does account for the influence of creep on stress accumulation, but it also uses slip-weakening friction rather than rate-state.

Here, we explore the likely controls that frictional conditions, fault geometry, and accumulated elastic stresses have on these processes. We use dynamic rupture modeling incorporating rate-state friction, which allows for mode switching between aseismic and coseismic deformation, to calculate scenario ruptures. We integrate these with static boundary element

models, which allow for a physics-based assessment of interseismic stress evolution, to develop our pre-stress conditions and to account for rapid postseismic creep. While this study is focused on the Hayward Fault, our findings will enable more accurate scenario modeling and hazard analysis for earthquakes on other partially creeping faults, which include major faults close to large regional populations in California (e.g. the Calaveras, Rodgers Creek and Concord faults), as well as the possibility of a major earthquake rupture propagating through the central creeping segment of the San Andreas Fault.

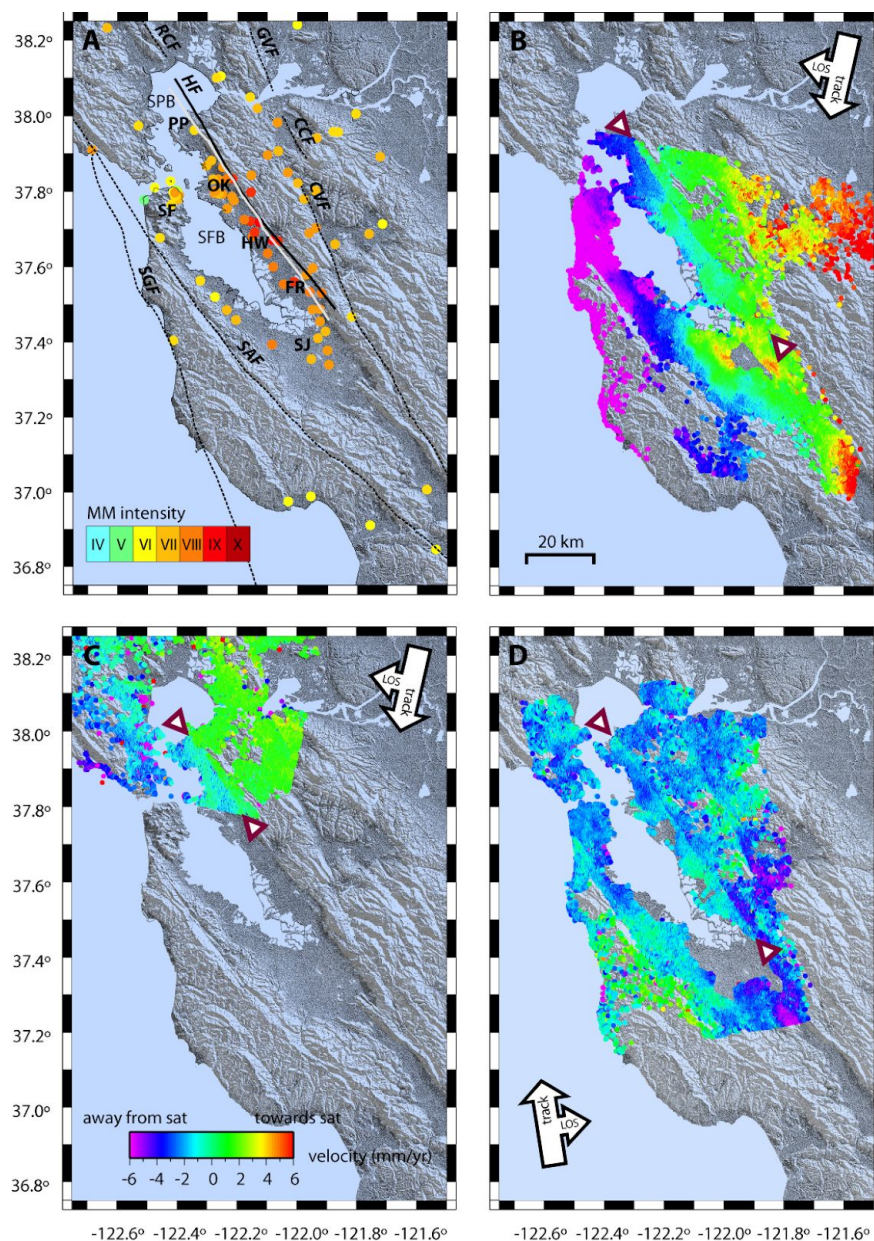


Figure 1: Summary maps of fault locations and data for the Hayward fault and San Francisco Bay Area. (A) Fault locations and observations of intensities from the 1868 Hayward earthquake (*Boatwright and Bundock, 2008*). The highest intensities are found in the central portion of the fault, implying that the majority of moment release occurred there. (B) ERS descending track 70 PS-InSAR velocities. (C) ERS descending track 342 PS-InSAR velocities. (D) Radarsat ascending track 38 PS-InSAR velocities. The location of the Hayward fault trace is indicated by red triangles. Abrupt cross-fault changes in PS-InSAR velocity indicate the occurrence of shallow fault creep. The reversal in the sense of velocity offset between descending and ascending datasets indicates that the creep is horizontal.

METHODS

In order to implement observation- and physics-based Hayward Fault behaviors in the interseismic, coseismic, and postseismic periods alike, we employed a three-step modeling process. First, we conducted static boundary element models of interseismic creep and stress evolution, based on GPS and InSAR velocity data constraining Hayward Fault creep. Next, we used the creep rate and distribution results of the static simulations as on-fault initial stress and friction inputs for dynamic finite element simulations of scenario Hayward Fault ruptures. Finally, we used the slip deficit accumulation rate from the (static) boundary element models and the coseismic slip distributions from the dynamic models to estimate the remaining slip deficit that could be released as rapid postseismic creep (afterslip). We describe each of these steps in more detail below.

Creep rate/distribution model setup

We produce multiple plausible distributions of creep and locking on the Hayward fault using a Markov Chain Monte Carlo estimation process guided by fit to geodetic deformation velocities, which we describe below.

Our geodetic data set consists of downsampled InSAR line-of-sight deformation velocities from two descending tracks of the ERS satellites and one ascending track of Radarsat-1 (after *Funning et al.*, 2009, Figure 1B-D) and GPS velocities from the regional BAVU compilation (*d'Alessio et al.*, 2005, Figure 2). We use estimates of regional fault slip rates estimated from these data in an earlier study (*Funning et al.*, 2009) to drive deep dislocations under the region's strike-slip faults. These, in turn, drive a boundary element model that uses a triangulated mesh of elements with diameters ~ 3 km in size to represent the complex surface of the Hayward fault (*Schmidt et al.*,

2005). In this boundary element model, fault elements can have one of two states – zero shear traction (i.e. zero frictional resistance), or zero displacement – which we use to represent creep and locking, respectively. For a given configuration of locked and creeping elements on the Hayward fault we use the poly3d software (*Thomas*, 1993) to calculate the distribution of creep on the fault surface and the expected surface deformation field at our geodetic observation locations. A penalty function based on the weighted residual sum of squares (WRSS) of the modeled displacements compared with the data is used to evaluate the model fit.

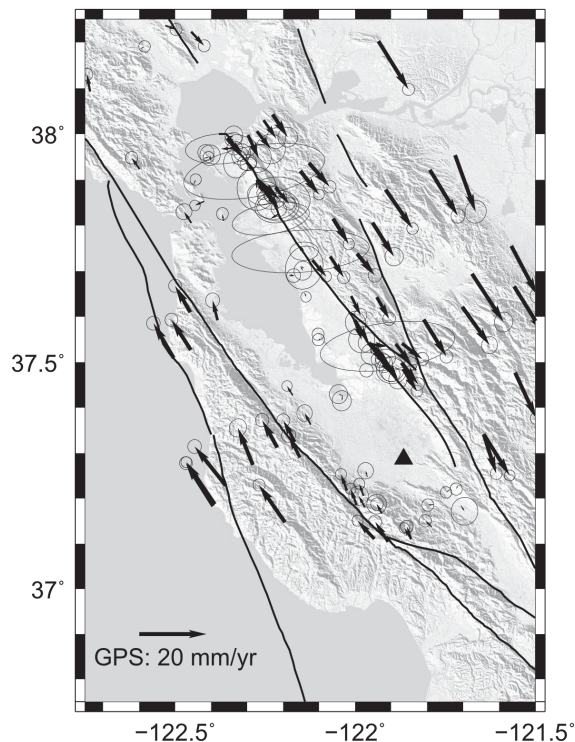


Figure 2 (left): GPS velocities from the BAVU compilation of campaign and continuous GPS data (after *d'Alessio et al.*, 2005). Velocities are plotted with respect to site LUTZ (black triangle).

From a starting model of 5 randomly selected locked elements, we use a modified Metropolis algorithm to sample the parameter space of possible locking distributions, and form a Markov chain of possible locking models. At each iteration of the model, a new trial configuration is tested, either randomly adding a locked element, removing an existing locked element, or changing the state (from locking to creeping, or vice-versa) of a neighbor of an existing locked element. If the new configuration produces an improved fit (reduced penalty), the change is automatically accepted. If the new configuration results in a greater penalty, then a random number test is used to choose whether the change is accepted, with a probability of acceptance that decreases as the penalty increases (*Metropolis et al.*, 1953; *Hastings*, 1970). If the change is rejected, then the unchanged model is retained. This process is repeated, and the configuration of locked and creeping elements varied, until the desired number of iterations is reached; we retain all of the accepted model configurations, along with the associated penalties and creep rate distributions. Known creeping fault elements, such as surface fault elements which include areas of known surface creep, or deeper fault elements that contain repeating earthquake sequences, are constrained to be creeping in all models.

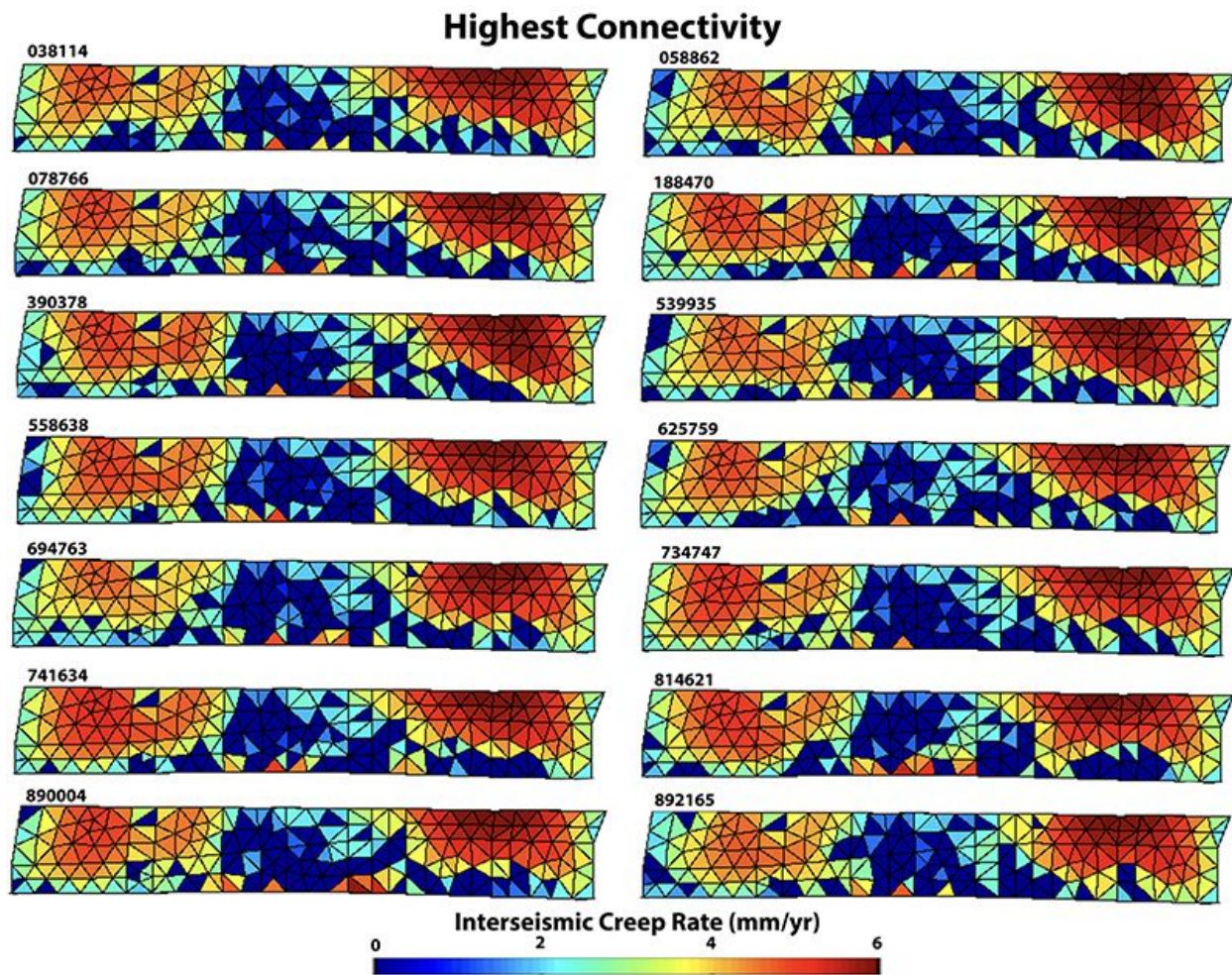


Figure 3: The 14 creep rate distributions with the highest connectivity between creeping and locked patches. The northern end of the fault is to the left.

In this study, we generate 1 million sample models using this process. To account for model spin-up, we exclude the first 2000 samples from consideration; after 2000 samples, the model configuration is in the region of parameter space where models that fit the data well are located.

In order to select locking configurations for modeling, we drew example model configurations in which the distribution of locked elements were more connected (more elements with edges in common) and more disconnected (fewer elements with edges in common). We selected 14 examples of each (Figures 3 and 4), and converted the corresponding creep rate distributions for these 28 models to slip rate deficits by differencing them from the basal Hayward fault driving dislocation rate (9.5 mm/yr). In this way, elements that are locked accumulate a slip deficit at the driving dislocation rate, whereas elements that are creeping accumulate proportionately less slip deficit, based on creep rate.

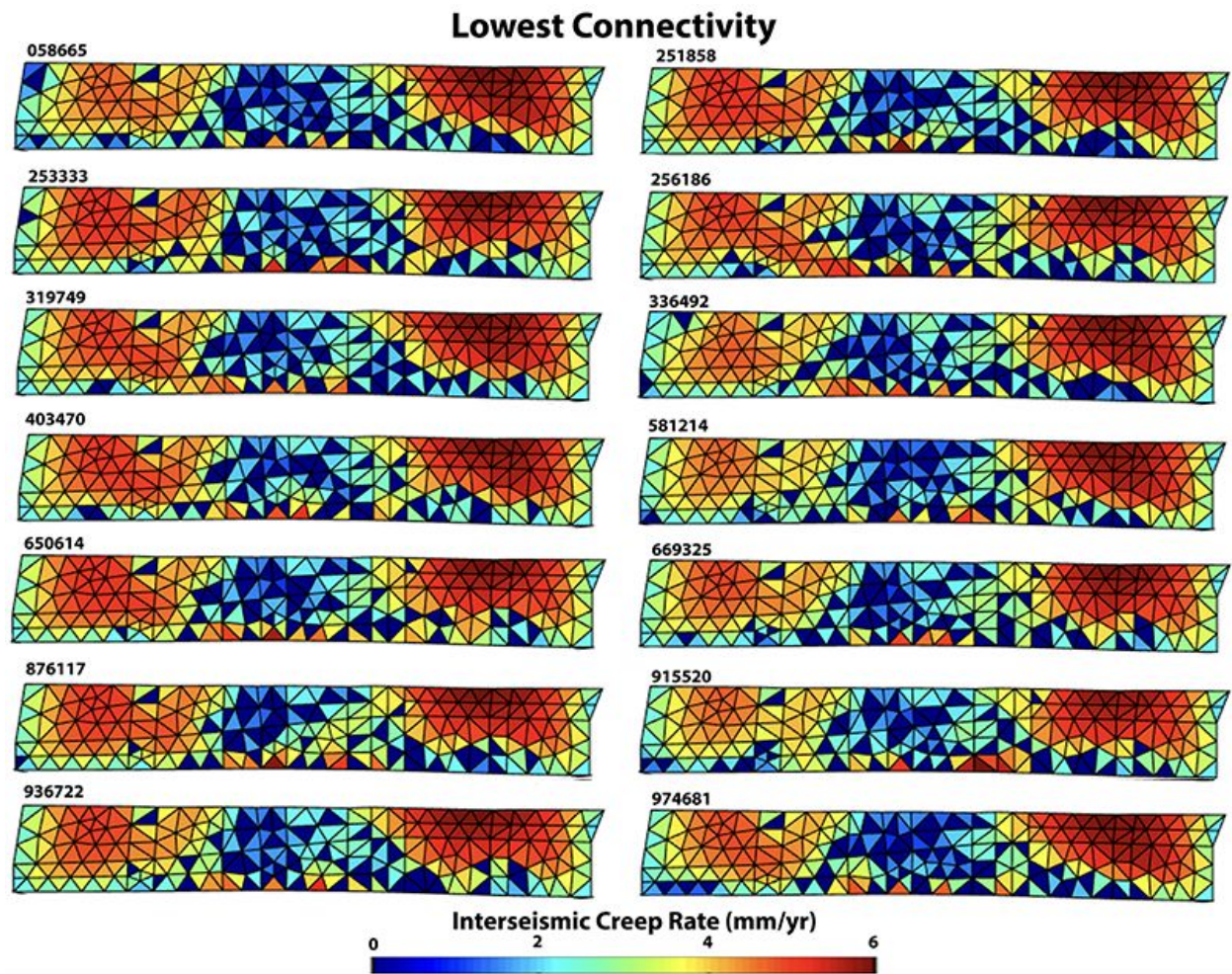


Figure 4: The 14 creep rate distributions with the lowest connectivity between creeping and locked patches. The northern end of the fault is to the left.

Dynamic rupture model setup

We generated the 3D tetrahedral finite element mesh for our dynamic rupture simulations using the commercial software Trelis. We used the same on-fault node coordinates to designate the fault geometry as in the boundary element models of interseismic and postseismic stress evolution, to ensure compatibility between the modeling methods, as well as to eliminate any possible effects of variable fault geometry. However, we created the finite element mesh at much higher resolution (~ 200 m element edges, as opposed to ~ 2 km) in order to adequately capture the rupture process. Figure 5 compares the fault geometries and grid resolutions for the inter-/post-seismic and dynamic models.

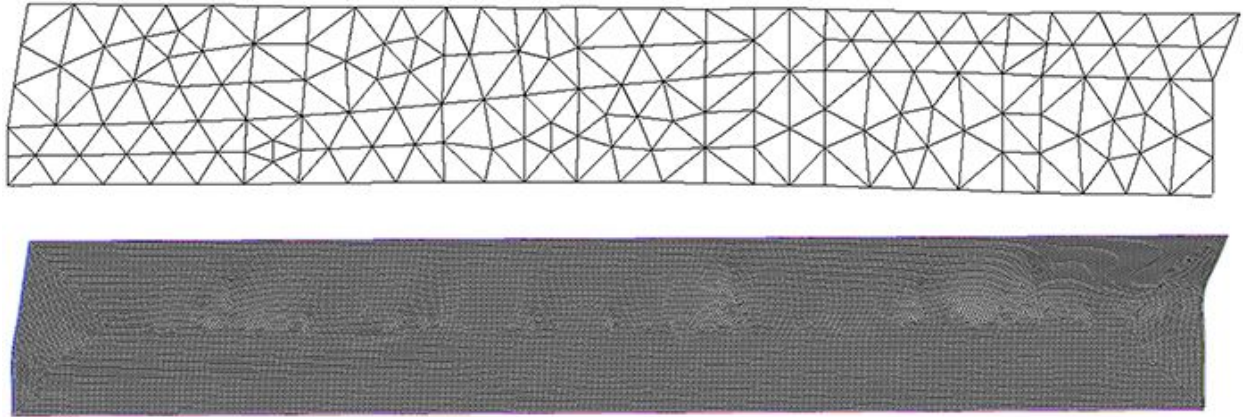


Figure 5: Comparison between the boundary element mesh for our static interseismic and postseismic models (top) and the finite element mesh for our dynamic coseismic rupture simulations (bottom).

We conducted the dynamic rupture simulations using the 3D finite element software FaultMod [Barall, 2009], which has consistently performed well in the Southern California Earthquake Center’s dynamic rupture code verification exercise [Harris *et al.*, 2009; Harris *et al.*, 2018]. We embed the model fault in a fully elastic homogeneous half space and implement rate-state friction with an aging law [Dieterich, 1978; Ruina, 1983]. We nucleate the simulated ruptures by raising the shear stress above the level required for failure, and forcing propagation over an area large enough to allow sustained rupture beyond that area. We list our material, frictional, and nucleation parameters in Table 1.

Both the initial frictional conditions and initial stresses for our dynamic models come from the static models described above, though we implemented these two conditions in separate ways. Creep versus locking is a simple toggle. We assigned rate-weakening behavior to elements determined to be locked in the static models, which means that these parts of the fault weaken further as they slip faster. For creeping elements, we either assigned rate-strengthening behavior, in which the fault actively resists slip as rupture attempts to propagate into it, or rate-neutral behavior, in which the fault neither weakens nor strengthens. We conducted two separate sets of models, one with creeping patches as rate-strengthening and another with creeping sections as rate-neutral; we did not mix these two behaviors in any single model.

Table 1. Physical and computational parameters.

Shear stress	21.758 MPa max, 12.758 MPa min
Normal stress	57.6120 MPa
a	Locked: 0.008 Rate strengthening: 0.014 Rate neutral: 0.012
b	0.012
μ_0	0.6
V_0	1×10^{-6}
D_c	0.02330 m
Y_{init}	0.135524
P wave velocity	6000 m/s
S wave velocity	3464 m/s
Density	2670 kg/m ³
Element size	200 m in the near field, 600m in the far field
Nucleation radius	2000 m
Nucleation shear stress	58.435 MPa

The initial on-fault stresses in our dynamic simulations scale based on the creep rates from the static interseismic simulations. For elements with zero creep rate, we assigned the maximum possible dynamic stress drop: 9 MPa, based on the average for small earthquakes on the Hayward Fault [Hardebeck and Aron, 2009]. For elements that creep at or faster than the 9.5 mm/yr basal driving rate from the static simulations described above, we assigned 0 MPa potential dynamic stress drop, under the assumption that these portions of the fault release all of their stored shear stress aseismically. For all creep rates between these two extremes, we assigned a proportionate amount of potential dynamic stress drop.

We conducted dynamic rupture simulations based on 28 different creep rate realizations from the static models described above: the 14 cases with the most consolidated (“high connectivity”) creeping and locked patches, and another 14 cases with more discontinuous (“low connectivity”) mixtures of creeping and locked elements. For each of these 28, we ran two sets of models, one with rate-strengthening friction in the creeping patches and one with rate-neutral friction in the creeping patches. In addition to these 56 simulations, we tested two cases in which we parameterized creeping patches with rate-strengthening or rate-neutral friction but did not reduce initial shear stress on these patches, and one case in which we set assumed all stress was released on creeping patches but still parameterized them as rate-weakening, in order to test the

effects of stress release and frictional contrast separately from one another. Lastly, we tested a single case with no creep effects whatsoever, to isolate any possible effects of fault geometry.

In order to prepare the dynamic rupture simulation results for the afterslip modeling process described below, we had to convert back from the fine-scale grid of these models to the coarser grid of the static models. We did so by averaging the slip and stress values of all the dynamic simulation nodes within a given element from the static simulations. Some of the detail of the final slip and stress distributions is lost in this manner, but this only affects second-order features of the model results, and still captures the effects of fundamental rupture behaviors.

Afterslip model setup

The next step is to estimate the afterslip that we expect following the earthquake for each of our model configurations. Our major assumption here is that the remaining slip deficit on the creeping parts of the fault following the earthquake will be released as afterslip. We make this estimate by first calculating the time it would take to accumulate a slip deficit equal to the maximum slip in each coseismic slip model. In order to avoid any bias imparted by the forced nucleation of the earthquake, we exclude the six fault elements in the immediate vicinity of the nucleation hypocenter from this estimation. Next, we use the 'slip deficit accumulation time' to calculate the total remaining slip deficit on each creeping element in each model. To make the results more comparable from model to model, we normalize each one by its maximum coseismic slip, and estimate the potential afterslip for each model as a percentage of that maximum.

RESULTS

Creep rate and distribution results

We show representative samples of a well-connected locking model and a disconnected model in Figure 6a and b (respectively), along with the resulting distributions of creep rates. Across all models obtained in our Markov chain sampling process, the greatest density of locked elements is located in the central portion of the fault, where surface creep rates are observed to be low (e.g. McFarland et al., 2016). The creep rate distributions show broadly similar patterns, with higher creep rates located at shallow depths towards the NW and SE ends of the fault, and lower creep rates in the central portion of the fault, where the greatest densities of locked elements are obtained. We find that a wide range of possible locking distributions, both connected and disconnected, give rise to similar patterns of creep rate that have similar fits to the data (i.e. similar values of the penalty function).

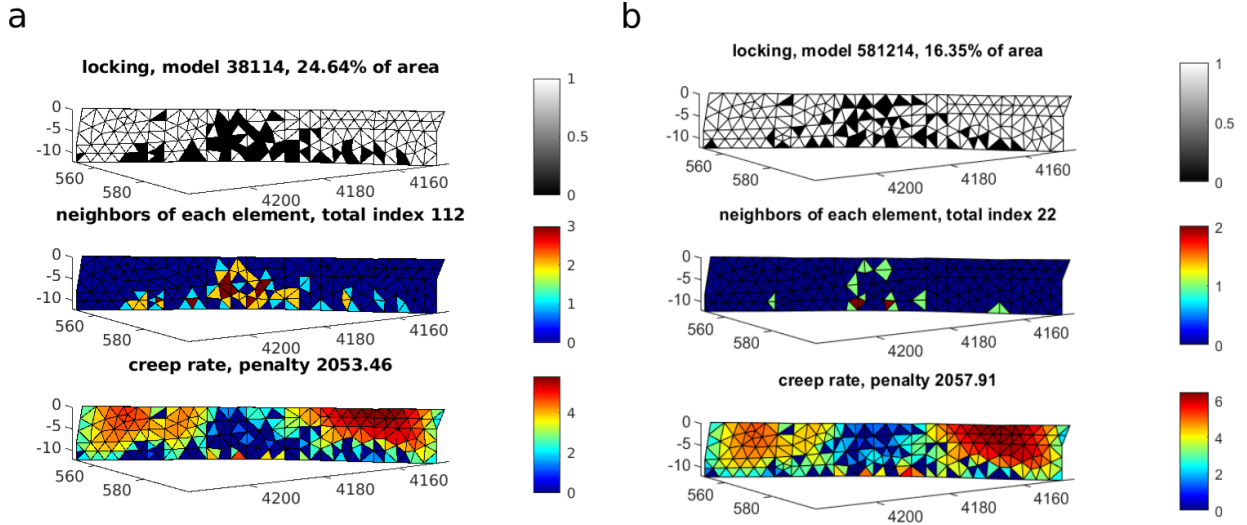


Figure 6: Examples of locking and creep rate distributions for the Hayward fault for (a) a well-connected model (i.e. a model whose locked elements are more connected), and (b) a disconnected model (i.e. a model whose locked elements are more disconnected). *Top row:* Distribution of locked (black) and creeping (white) elements. In general, we obtain a higher density of locked elements in the central portion of the Hayward fault in all models. *Middle row:* Number of neighbors for each element, a measure of element connectivity. Plotted are the number of elements that share a common edge with each element in turn; the total number of neighbors for all elements is an index used to distinguish between well connected models (index > 110) and disconnected models (index < 25). *Bottom row:* Distribution of creep rates, estimated in our boundary element model. Locked elements have a zero creep rate, and act to suppress creep rate on nearby creeping elements. Overall, we see similar features in all of our models – higher creep rates at the ends of the fault, especially at shallower depths, and lower creep rates in the central portion of the fault, where the majority of locked elements are located.

Dynamic rupture results

All of our simulations designed to test the effect of a single type of heterogeneity on rupture length did propagate through the entire model Hayward Fault. However, the amount of slip in the resulting rupture was sensitive to changes in frictional properties or stress accumulation. Our fully rate-weakening model with no shear stress reduction due to creep (Figure 7a) had the most slip, as well as the smoothest slip distribution. The model with no reduced shear stress and creeping sections parameterized as rate-strengthening (Figure 7b) produced less slip than the one with no stress release and rate-neutral creeping sections (Figure 7c). Slip in the case with no frictional contrast but reduced shear stress in the creeping sections (Figure 7d) was between the rate-strengthening and rate-neutral cases. Despite the difference in overall magnitude of slip in these last three cases, the patches of higher and lower slip are in the same places for all three, and correspond directly with the pattern of interseismic creep versus locking.

However, none of our dynamic rupture simulations which incorporate rate-strengthening or rate-neutral friction as well as reduced initial shear stress on creeping fault patches propagate

through the entire model Hayward Fault. In all cases, the creeping sections on the northern and southern ends of the fault confine coseismic rupture to the central section of the fault, from Oakland to Fremont. Our largest model rupture is a M7.16 and our smallest is a M6.71; this magnitude range, as well as the location of significant coseismic slip in our simulations, is consistent with existing interpretations of the 1868 Hayward Fault earthquake [e.g. *Yu and Segall, 1996; Boatwright and Bundock, 2008; Hough and Martin, 2015*].

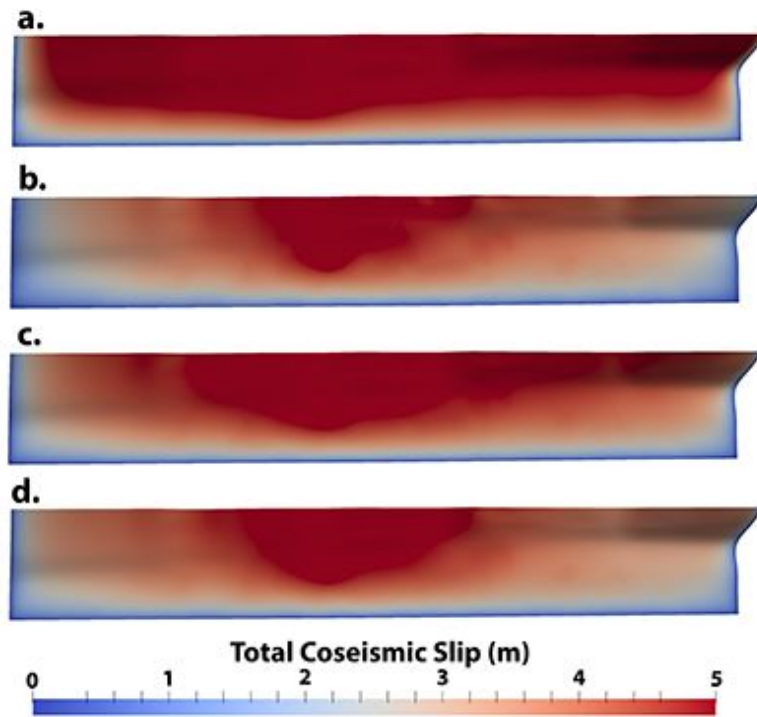


Figure 7 (left): Slip distributions from dynamic rupture simulations which isolate individual parameters that may affect our complex simulations. a. No stress or friction contrast, isolating fault geometry. b. Creeping sections parameterized with rate-strengthening friction, but no shear stress reduction. c. Creeping sections parameterized with rate-neutral friction, but no shear stress reduction. d. Creeping sections parameterized with reduced shear stress, but no frictional contrast. These examples are based on creep distribution 038114 (see Figure 3.)

Our dynamic rupture simulations based on the interseismic slip distributions with the most continuity in locked sections produced ~35 km long, M6.95-M7.03 ruptures when we parameterized creeping sections with rate-strengthening behavior (Figure 8), and ~55 km, M6.99-M7.14 ruptures when parameterized with rate-neutral behavior (Figure 9). Rupture in rate-strengthening models remained confined to locked or low creep rate fault patches, while rupture in rate-neutral models was able to bilaterally propagate further into creeping sections with higher creep rates. Changes in the smaller-scale details of the creep distribution did not affect the first-order feature of rupture length, for either frictional behavior. The specific characteristics of each interseismic creep distribution are more visible in the second-order details of the coseismic slip distributions. The highest slip occurred in fully locked fault patches, with localized low-slip patches coinciding with patches of higher creep rate. This effect is more pronounced in rate-strengthening models than in rate-neutral ones.

Our dynamic simulations based on the interseismic models with the least continuity in the locked sections produced shorter ruptures compared to the more continuous creep and locking

distributions. Simulations with rate-strengthening friction in the creeping sections produced ~25 km, M6.20-M6.89 ruptures (Figure 10) and simulations with rate-neutral friction produced ~45 km, M6.98-M7.06 ruptures (Figure 11). Other than the difference in rupture size, the basic characteristics of these sets of models are consistent with the more continuous models described above. There are still no first-order differences in rupture length and location; the differences between interseismic models are still more visible as patches of high and low slip within the rupture zone, which are again more pronounced in rate-strengthening models.

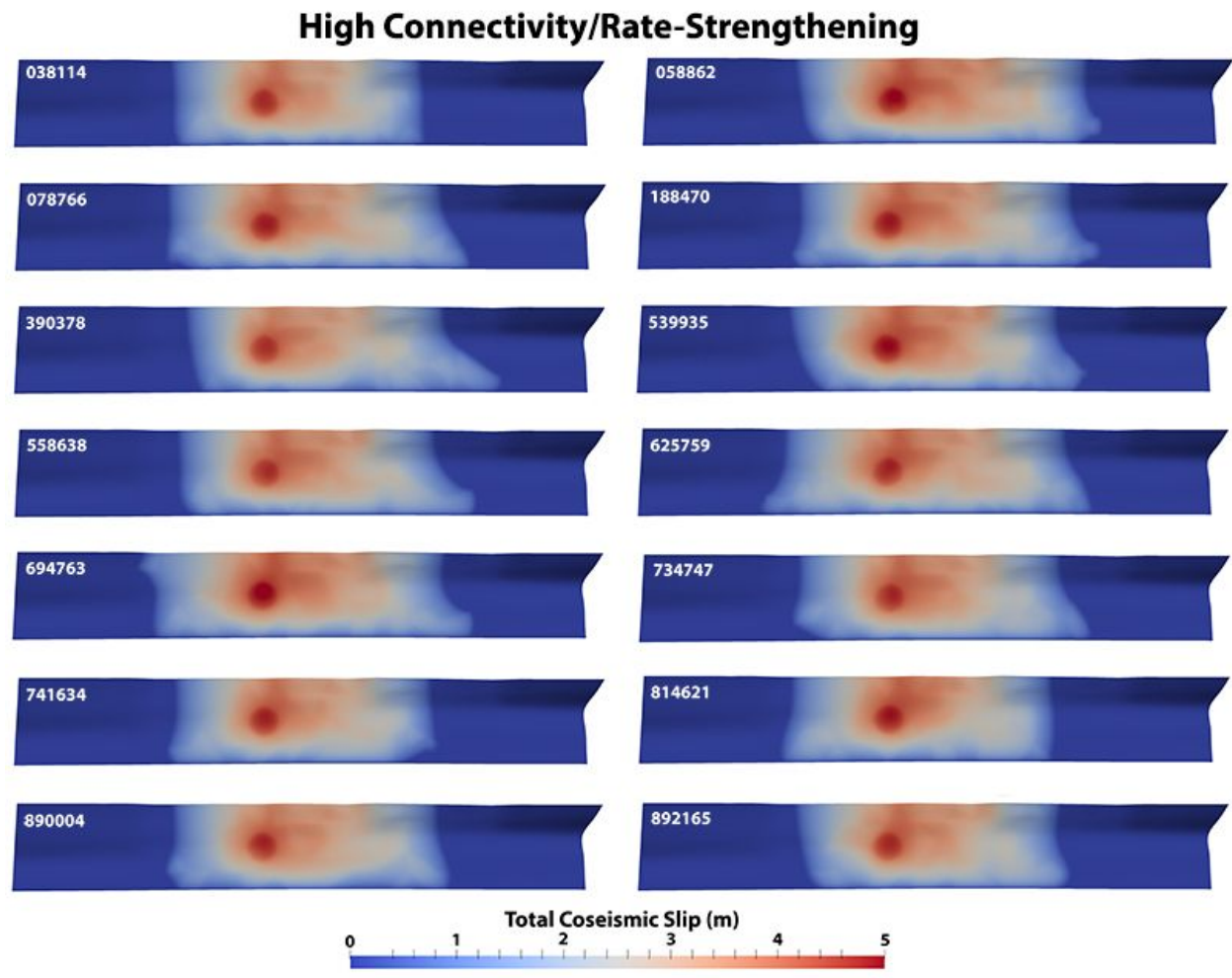


Figure 8: Slip distributions from dynamic rupture simulations based on the high connectivity interseismic slip rate models shown in Figure 3, with creeping sections parameterized with rate-strengthening friction. The northern end of the fault is to the left. The circular high slip patch represents our forced nucleation zone.

High Connectivity/Rate-Neutral

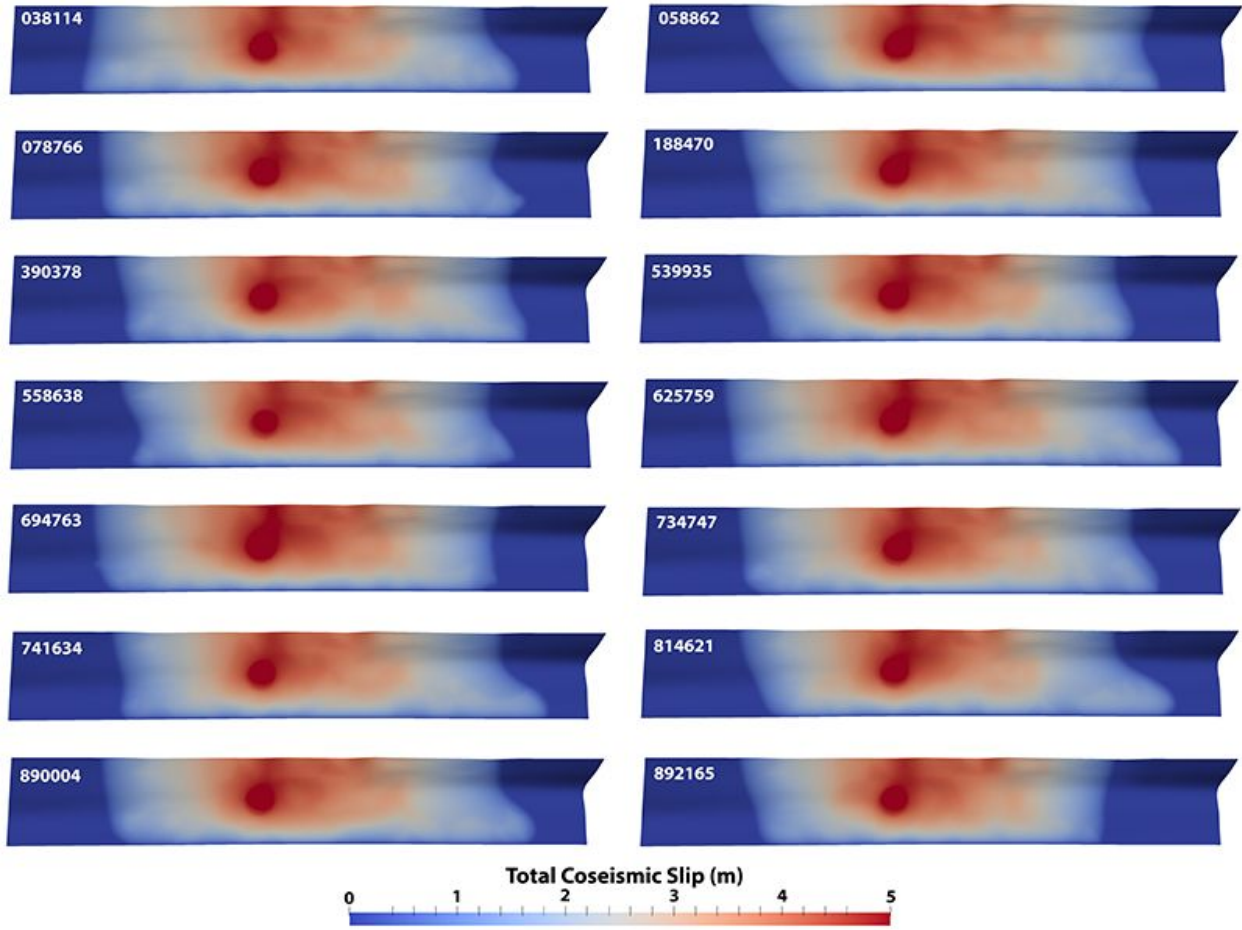


Figure 9: Slip distributions from dynamic rupture simulations based on the high connectivity interseismic slip rate models shown in Figure 3, with creeping sections parameterized with rate-neutral friction. The northern end of the fault is to the left. The circular high slip patch represents our forced nucleation zone.

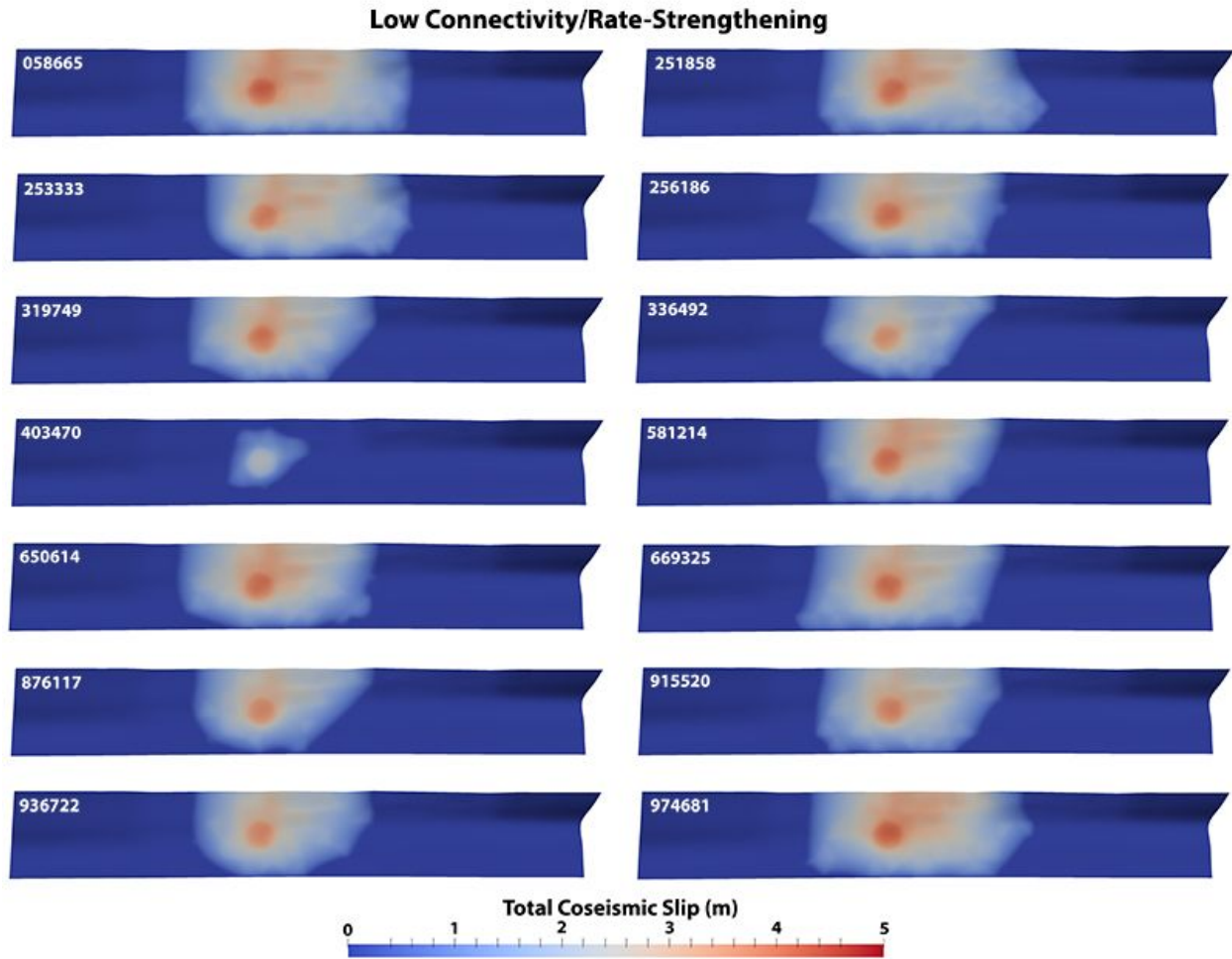


Figure 10: Slip distributions from dynamic rupture simulations based on the low connectivity interseismic slip rate models shown in Figure 4, with creeping sections parameterized with rate-strengthening friction. The northern end of the fault is to the left. The circular high slip patch represents our forced nucleation zone.

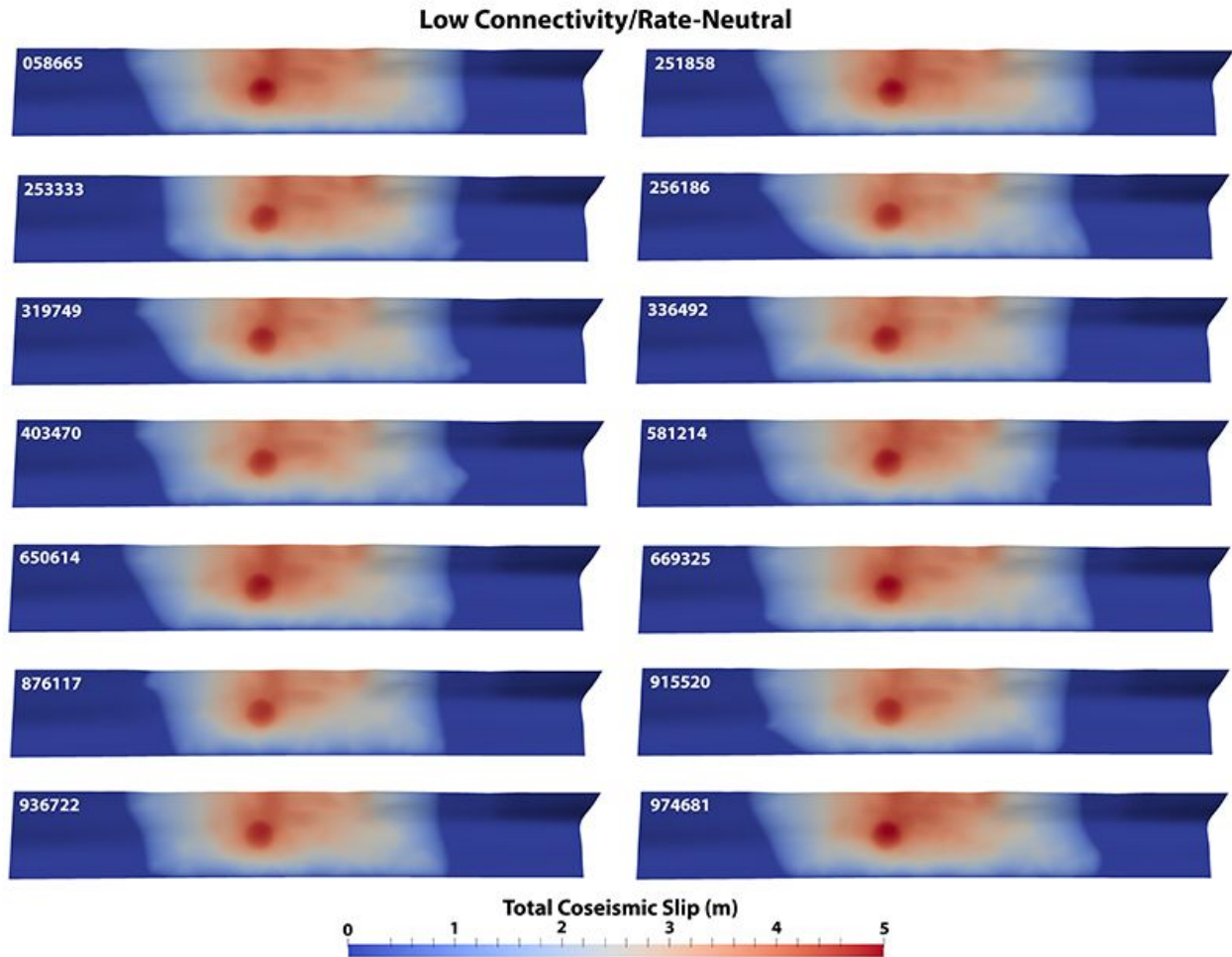


Figure 11: Slip distributions from dynamic rupture simulations based on the low connectivity interseismic slip rate models shown in Figure 4, with creeping sections parameterized with rate-neutral friction. The northern end of the fault is to the left. The circular high slip patch represents our forced nucleation zone.

Afterslip results

Representative examples of afterslip models for each combination of model connectedness (well connected vs disconnected) and frictional conditions (rate strengthening vs rate neutral) are shown in Figure 12. All models show that in some areas of the fault, most notably the lower edge and the fault ends, a slip deficit of up to 80% of the maximum coseismic slip could be released as afterslip. Similarly, in all models the area of highest coseismic slip in the central portion of the fault has little to no remaining slip to be released as afterslip. Beyond those similarities, we can identify some differences between the different categories of models.

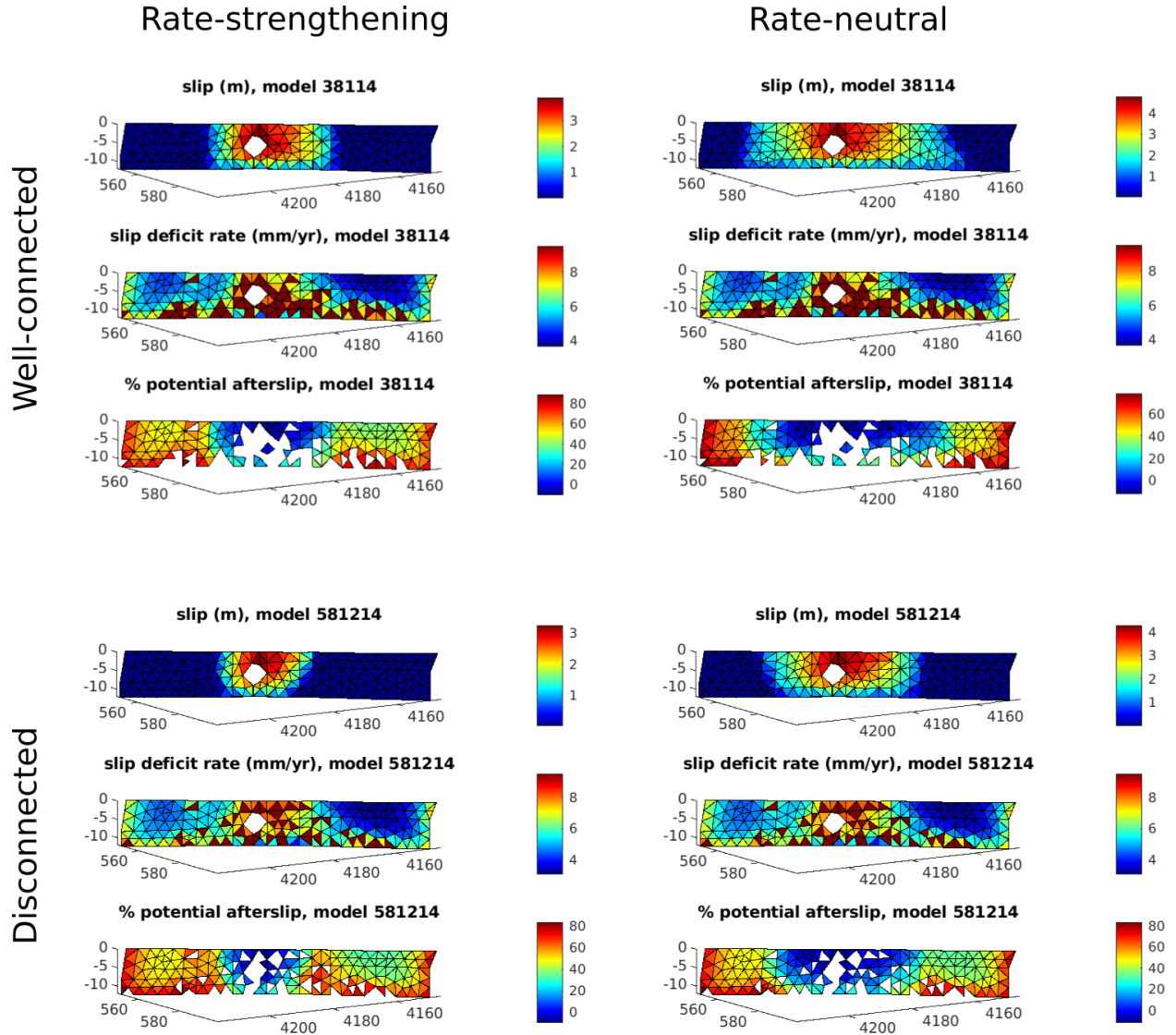


Figure 12: Examples of potential afterslip for different combinations of model connectedness (rows) and frictional conditions (columns). Each combination includes three subfigures – *top*: coseismic slip from the dynamic rupture simulation, with nucleation elements excluded; *middle*: estimated slip deficit rate from the creep/locking estimation process, assuming a long-term slip rate of 9.5 mm/yr; *bottom*: estimated potential afterslip (unreleased accumulated slip deficit) as a percentage of maximum coseismic slip. Locked fault elements are excluded from the afterslip plot. Note that well-connected models have longer coseismic slip zones, and thus narrower afterslip zones than disconnected models, as do rate-neutral friction models compared with rate-strengthening friction models. We expect higher amounts of afterslip (up to 80% of maximum coseismic slip) around the lower edge and ends of the fault than at the surface, but up to 50% of the maximum coseismic slip could be released in areas where there was significant interseismic creep (e.g. Figure 6), to the NW and SE of the main coseismic slip zone.

The most prominent differences between models are in the relative dimensions of the coseismic slip zone in the center of the fault, and the zones of afterslip that flank that coseismic slip zone to the NW and SE. In general, we obtain longer coseismic zones/narrower afterslip zones for the well-connected locking models, compared with the disconnected models. Models with rate-neutral friction also show narrower areas of afterslip and a longer zone of coseismic slip than those that use rate-strengthening friction. These two effects – longer ruptures resulting from a greater density of locked elements and rate-neutral friction decreasing the impedance of rupture through creeping elements – combine, such that the narrowest afterslip zones are found in models that combine well-connected locking zones with rate-neutral friction (e.g. Figure 12, top right). Conversely, the largest afterslip zones (e.g. Figure 12, bottom left) result from models that combine disconnected locked elements and rate strengthening friction.

Another difference between models employing rate-strengthening friction and their rate-neutral counterparts, is that rate-strengthening models show a ‘halo’ of high predicted afterslip (up to 60-70% of the maximum coseismic slip) surrounding the coseismic slip zone. In the disconnected models, this is found on both sides of the central coseismic zone; in the well-connected models, this is more prominent on the NW side.. Under rate-neutral friction, most models rupture through those zones, and thus the expected afterslip is substantially lower adjacent to the coseismic slip zone. With or without the halo effect, the areas of high shallow interseismic fault creep midway between the central coseismic slip zone and the NW and SE ends of the fault in all models (e.g. Figures 3 and 4), could potentially release ~40–50% of the maximum coseismic slip as afterslip, which although lower than the expected amounts at the ends and lower edge of the fault, would still represent a significant afterslip hazard.

DISCUSSION

Dynamic rupture discussion

Our simpler simulations in which we isolated the effects of fault geometry, frictional contrast without reduced shear stress, and reduced shear stress without frictional contrast (Figure 7) provide much of the information necessary to interpret our models which incorporate both stress and frictional heterogeneity. The fact that our simplest model with homogeneous initial stresses and homogeneous rate-weakening friction has smooth rupture propagation across the entire fault and produces a largely symmetrical slip distribution suggests that the Hayward Fault’s geometry is not a major factor in rupture pattern and cessation. In contrast, the fact that both models which isolate frictional contrast without stress reduction, and the one which isolates stress reduction without frictional contrast, also have rupture through the entire fault implies that the combination of these two effects is necessary to limit rupture propagation as in our fully complex models (Figures 8 through 11).

Both frictional resistance or reduced shear stress can create a barrier to rupture by rebalancing the energy budget of the rupture front toward fracturing into unfavorable territory, rather than sliding along an existing crack and radiating seismic energy [e.g. *Kanamori and Rivera, 2006*]. (Note that, while the original definition of the energy budget of a rupture is framed in terms

of slip-weakening friction, *Ryan and Oglesby* [2014] show that rupture front behavior under rate-state friction is comparable. This is particularly true at full coseismic rupture velocities, which is true of our model rupture fronts as they propagate through locked fault sections and approach creeping ones.) Even if this effect does not entirely stop the rupture front, a temporarily unbalanced energy budget through a frictionally resistant or low shear stress fault patch can still result in a localized patch of lower slip. Many previous rupture simulation studies illustrate this effect for patches of reduced shear stress [e.g. *Andrews and Barall*, 2011; *Richards-Dinger and Dieterich*, 2012; *Fang and Dunham*, 2013; *Lozos et al.*, 2015b]. Previous work on dynamic rupture propagation through partially creeping faults also describes this effect when the creeping sections are parameterized within slip-weakening friction [e.g. *Lozos et al.*, 2015a; *Harris et al.*, submitted] as well as within rate-state friction [e.g. *Lapusta and Liu*, 2009; *Lozos*, 2013].

In all of our Hayward Fault rupture simulations, the central locked (rate-weakening) section of the fault fully ruptures (see figures 8-11). How far rupture is able to propagate beyond this locked patch depends on how frictionally resistant the surrounding creeping sections are, how connected the central locked section is to smaller locked patches beyond it, and how many smaller creeping patches exist within the central locked section.

The correlation between rupture length and frictional parameterization is straightforward; by definition, rate-strengthening behavior actively resists slip, while rate-neutral behavior neither promotes nor resists [*Dieterich*, 1978; *Ruina*, 1983]. Thus, rupture is able to propagate further into rate-neutral creeping sections than into rate-strengthening ones because its energy budget is merely not being provided with additional stress drop, rather than actively being resisted [e.g. *Lozos*, 2013].

As described above, small resistant patches on a fault - whether from frictional contrast, reduced shear stress, or both - can temporarily unbalance the rupture front's energy budget and produce local lows in slip. We see this effect in all of our dynamic simulations, where low slip areas within the central locked section correspond with small patches of low creep rate. This is more pronounced in models with rate-strengthening creeping patches, again because this frictional behavior actively resists slip while rate-neutral friction merely does not promote it. This effect is also more pronounced in the ruptures based on interseismic models with low connectivity in creeping and locked patches, since there are more and larger creeping intrusions into the locked central patch. This is enough to confine the rupture to a smaller area in these cases, as rupturing around and through these small creeping patches drains enough energy from the rupture front that it is already weaker by the time it reaches the creeping sections on either end of the fault, and is therefore not able to propagate as far into them.

The majority of the high-connectivity interseismic models have a smaller locked patch at the base of the southern (rightmost) creeping patch. However, only some of the dynamic simulations (such as numbers 558638, 861682, and 866385, see Figure 8) have rupture that continues through this section at depth. In these cases, this secondary locked zone is either more connected to the main one with fewer direct barriers to rupture, or there are fewer small creeping patches within the main locked zone, which keeps the rupture front more energetic as it proceeds to the south at depth. Even in these cases, the width of this locked extension is still small enough that the rupture front is not able to grow to a self-sustaining size underneath the large creeping zone, which leads to

rupture at depth also ceasing before it reaches the end of the fault. This effect is also consistent with previous work on partially creeping faults [e.g. *Lozos, 2013; Lozos et al., 2015a*].

Afterslip discussion

In many ways, our models of potential Hayward fault afterslip are a zero-sum proposition compared with our dynamic rupture models, given the finite slip deficit budget. Factors that act to enlarge the coseismic slip zone will act to narrow the afterslip zones on the fault, by releasing accumulated slip deficit coseismically that would otherwise be released aseismically as afterslip. Thus, well-connected fault models in which coseismic slip is sustained for longer by greater numbers of locked fault elements, and in which sequential rupture of locked elements is favored by their connectivity, typically have narrower aftershock zones. Similarly, models employing rate-neutral friction in creeping fault areas demonstrate reduced impedance to ruptures propagating into those areas, compared with rate-strengthening friction. These models also show expanded coseismic slip zones and narrower afterslip zones. These effects can be combined, such that well-connected rate-neutral models show overall the narrowest afterslip zones, and disconnected rate-strengthening models show the largest.

Of the two effects, we interpret the frictional condition as having the stronger influence on the afterslip distribution and magnitude. We mentioned above the ‘halo effect’ seen in rate-strengthening models, of elevated percentages of potential afterslip in a narrow zone surrounding or flanking the coseismic slip zone. With rate-strengthening friction suppressing coseismic slip in these areas, but high slip deficit accumulation due to proximity to the locked elements of the central locked zone of the fault, the ‘halo’ retains a large slip deficit after the earthquake. Notably this higher proportion of unreleased slip deficit could be released at shallow depths, posing an increased hazard from elevated shallow afterslip. This effect presents a significant epistemic uncertainty, of up to 20% of maximum coseismic slip, that depends on the choice of friction parameters. Therefore it is crucial for the accuracy of such afterslip models, if they are to be used in a predictive context, to place constraints on the appropriate frictional model ahead of time.

Implications for Hayward Fault hazard

Based on our dynamic rupture simulations, we think it is unlikely that coseismic rupture can propagate through the entire Hayward Fault, so long as the distribution of creeping and locked patches remains in place. Even in our most permissive models (high connectivity between locked patches and rate-neutral friction in creeping zones), the combination of lower initial shear stress due to interseismic strain release from creep, and loss of rupture energy as the fault does not weaken in creeping sections, prevents rupture from reaching either end of the fault. That said, our least permissive models (low connectivity between locked patches and rate-strengthening friction in creeping zones) still produce earthquakes in the M6.7 - M6.8 range. This is comparable to the widely damaging Hayward Fault earthquake of 1868 [e.g. *Boatwright and Bundock, 2008; Hough and Martin, 2015*]. A similarly sized earthquake would be devastating to the modern Bay Area due to the Hayward Fault’s location and geologic setting [e.g. *Detweiler and Wein, 2018*].

In addition to limiting the size of potential ruptures on the Hayward Fault alone, the creeping sections on the northern and southern ends of the fault may also make multi-fault

ruptures involving the Hayward less likely. The Hayward Fault connects to the Rodgers Creek Fault to the north via a 10° bend under San Pablo Bay [Watt *et al.*, 2016] and to the Calaveras Fault to the south via a complex subsurface splay [Chaussard *et al.*, 2015]. However, the ~30 km long creeping sections on either end of the Hayward Fault in all of our interseismic creep models effectively impose much larger separation between the seismogenic portions of the Hayward and the Calaveras or Rodgers Creek faults. Even in our most permissive, longest-rupture models, coseismic slip stops ~15 km from the ends of the fault, a distance considerably larger than the majority of gaps in strike-slip rupture traces [Wesnowsky, 2008]. Furthermore, the high-stress stopping phase associated with rupture hitting a sharp barrier or fault end, which is a large factor in initiating secondary rupture beyond a fault end or barrier [e.g. Harris and Day, 1993; Oglesby, 2008; Lozos *et al.*, 2011], is weaker when a rupture slows to a stop due to losing energy (as it does in our Hayward Fault simulations), and is therefore less likely to cause a new nucleation on a distant fault patch. Our interpretation that earthquakes which initiate on the main locked patch of the Hayward Fault are unlikely to propagate onto neighboring faults in a single event is consistent with the work of Harris *et al.* [submitted], who simulated dynamic ruptures on the Rodgers Creek-Hayward-Calaveras system using slip-weakening friction.

Although dynamic ruptures are either arrested or peter out in the creeping portions of the Hayward fault, in all of our models there remains a significant unreleased slip deficit in those areas – 40% of the maximum coseismic slip at the surface, and possibly larger percentages at depth. In some cases, such as models combining disconnected locked elements and rate-strengthening friction, the percentage could be 60% or higher at the surface. If, as we assume, this unreleased slip deficit is manifest as afterslip on the Hayward fault in the days or weeks following an earthquake, the hazard posed by this afterslip could be substantial. Using the maximum slip estimates from our coseismic modeling, of 3–5 m, we would expect afterslip of at least 1.2–2.0 m at the surface, sufficient to break fault-crossing infrastructure at locations that did not experience coseismic surface rupture.

In addition to posing a surface offset hazard on its own, afterslip may also increase the loading speed on unruptured locked patches of the Hayward Fault, or on other adjacent and nearby faults. On the Hayward Fault itself, remaining locked patches (such as the one underneath the southernmost/ rightmost creeping section) may be likely locations for significant aftershocks, as they are characterized by rate-strengthening behavior and surrounded and loaded by rapid afterslip. The same mechanism drives small repeating earthquakes on partially creeping faults even at normal interseismic slip rates [e.g. Nadeau and Johnson, 1998], so we expect that rapid afterslip may be able to drive both small and large residual locked patches to failure. Similarly, rapid postseismic creep on the Hayward Fault may cause additional static stress transfer to the adjacent Calaveras and Rodgers Creek faults, including the locked sections of these faults, beyond that resulting from the coseismic slip on the Hayward fault. With this in mind, we suggest that a sequence of events on the Hayward and its neighboring faults is more physically plausible than a single multi-fault rupture through this system.

CONCLUSIONS

Using a hybrid static interseismic/postseismic and dynamic coseismic modeling technique, we find that sections of persistent aseismic creep are likely to confine dynamic rupture on the Hayward Fault to a central locked fault section between Oakland and Fremont. These creeping sections pose a barrier to throughgoing rupture both due to the fact that creep releases some shear stress in the interseismic period, and to frictional resistance. Thus, we suggest that an end-to-end rupture of the Hayward Fault is unlikely (as is multi-fault rupture involving the adjacent Calaveras and Rodgers Creek faults), while upper-M6 range 1868-type events may be more typical. However, our postseismic models all show potential for significant and extensive afterslip along all sections of the fault which did not rupture coseismically, as well as for some parts of the fault that did. Thus, the entire Hayward Fault still presents a significant surface offset hazard. We also suggest that afterslip on the Hayward Fault may accelerate stress transfer to other nearby partially creeping faults, including the locked sections of those faults.

We note that the current model recurrence intervals required to produce the amounts of coseismic and postseismic slip in our simulations (~ 300 -550 years) are in the range of a factor of 2-3 times larger than inferred for the real Hayward Fault (~ 120 -180 years, *Lienkaemper and Williams, 2007*). This discrepancy is likely an effect of our choice of maximum coseismic stress drop in our dynamic rupture simulations; while 9 MPa is consistent with Hayward Fault microseismicity [*Hardebeck and Aron, 2009*], larger earthquakes which sample more of the fault plane will also sample a broader stress distribution that may average to an overall lower average stress drop. We plan to experiment with lower dynamic stress drop values in our coseismic rupture simulations, until we find a value which produces both ruptures that are consistent with interpretations of the 1868 earthquake and recurrence intervals that are consistent with paleoseismic and geodetic interpretations.

REFERENCES

- Aagaard, B. T., R. W. Graves, D. P. Schwartz, D. A. Ponce, and R. W. Graymer (2010a), Ground-motion modeling of Hayward fault scenario earthquakes, Part I: Construction of the suite of scenarios, *Bulletin of the Seismological Society of America* 100(6), 2927-2944, doi: 10.1785/0120090324.
- Aagaard, B. T., R. W. Graves, A. Rodgers, T. M. Brocher, R. W. Simpson, D. Dreger, N. A. Petersson, S. C. Larsen, S. Ma, and R. C. Jachens (2010b), Ground motion modeling of Hayward fault scenario earthquakes, Part II: Simulation of long-period and broadband ground motions, *Bulletin of the Seismological Society of America*, 100(6), 2945-2977, doi: 10.1785/0120090379.
- Aagaard, B. T., J. J. Lienkaemper, and D. P. Schwartz (2012), Probabilistic estimates of surface coseismic slip and afterslip for Hayward fault earthquakes, *Bulletin of the Seismological Society of America*, 103(3), 961-979, doi: 10.1785/0120110200.
- Andrews, D. J., and M. Barall (2011). Specifying initial stress for dynamic heterogeneous earthquake source models, *Bull. Seismol. Soc. Am.* 101, no. 5, 2408-2417, doi:10.1785/0120110012.

- Barall, M. (2009). A grid-doubling finite-element technique for calculating dynamic three-dimensional spontaneous rupture on an earthquake fault, *Geophys. J. Int.*, 178 (2), 845-859.
- Boatwright, J., and H. Bundock (2008), Modified Mercalli Intensity maps for the 1868 Hayward earthquake plotted in ShakeMap format, Open File Rep. 2008-1127, U.S. Geol.Surv., Menlo Park, Calif
- d'Alessio, M. A., I. A. Johanson, R. Bürgmann, D. A. Schmidt and M. H. Murray (2005), Slicing up the San Francisco Bay Area: Block kinematics and fault slip rates from GPS-derived surface velocities, *J. Geophys. Res.*, 110, B06403, doi:10.1029/2004JB003496
- Chaussard, E., R. Bürgmann, H. Fattahi, R. M. Nadeau, T. Taira, C. W. Johnson, and I. Johanson (2015), Potential for larger earthquakes in the east San Francisco Bay Area due to the direct connection between the Hayward and Calaveras faults, *Geophys. Res. Lett.*, 42, doi:10.1002/2015GL063575.
- Detweiler, S. T. and A. M. Wein (eds), 2018, The HayWired Earthquake Scenario— Engineering Implications, USGS Scientific Investigations Report 2017–5013–I–Q
- Dieterich, J. H. (1978), Time-dependent friction and the mechanics of stick-slip, *Pure. Appl. Geophys.*, 116, 790–806.
- Fang, Z. J. and E. M. Dunham (2013), Additional shear resistance from fault roughness and stress levels on geometrically complex faults, *J. Geophys. Res. Solid Earth*, 118, 3642–3654, doi:10.1002/jgrb.50262.
- Field, E. H., R. J. Arrowsmith, G. P. Biasi, P. Bird, T. E. Dawson, K. R. Felzer, D. D. Jackson, K. M. Johnson, T. H. Jordan, C. Madden, A. J. Michael, K. R. Milner, M. T. Page, T. Parsons, P. M. Powers, B. E. Shaw, W. R. Thatcher, R. J. Weldon, and Y. Zeng (2014), Uniform California Earthquake Rupture Forecast, version 3 (UCERF3) – the time-independent model, *Bull. Seismol. Soc. Am.*, 104, 1122–1180, doi:10.1785/0120130164.
- Floyd, M. A., R. J. Walters, J. R. Elliott, G. J. Funning, J. L. Svarc, J. R. Murray, A. J. Hooper, Y. Larsen, P. Marinkovich, R. Bürgmann, I. A. Johnason, and T. J. Wright (2016), Spatial variations in fault friction related to lithology from rupture and afterslip of the 2014 South Napa, California, earthquake, *Geophys. Res. Lett.*, 43, 6808–6816, doi:10.1002/2016GL069428.
- Funning, G. J., R. Bürgmann, A. Ferretti and F. Novali (2009), Mapping the extent of fault creep along the Hayward-Rodgers Creek-Maacama fault system using PS-InSAR, *Eos Trans. AGU*, 90(52), Fall Meet. Suppl., Abstract G34A-08.
- Funning, G. J. and R. Bürgmann (2014). An objective mechanical modelling approach for estimating the distribution of fault creep and locking from geodetic data, Abstract T41C-4658 presented at 2014 Fall Meeting, AGU, San Francisco, Calif., 15-19 Dec.
- Hardebeck, J. L., and A. Aron (2009), Earthquake stress drops and inferred fault strength on the Hayward fault, East San Francisco Bay, California, *Bull. Seismol. Soc. Am.*, 99, 1801–1814, doi:10.1785/0120080242.
- Harris, R.A., and S.M. Day, (1993), Dynamics of fault interaction: parallel strike-slip faults, *J. Geophys. Res.*, vol. 98, 4461-4472, doi:10.1029/92JB02272
- Harris, R. A., M. Barall, R. Archuleta, E. Dunham, B. Aagaard, J. P. Ampuero, H. Bhat, V. Cruz-Atienza, L. Dalguer, P. Dawson, S. Day, B. Duan, G. Ely, Y. Kaneko, Y. Kase, N. Lapusta, Y. Liu, S. Ma, D. Oglesby, K. Olsen, A. Pitarka, S. Song, and E. Templeton (2009), The SCEC/USGS Dynamic

- Earthquake Rupture Code Verification Exercise, *Seismological Research Letters*, 80(1), 119-126, doi: [10.1785/gssrl.80.1.119](https://doi.org/10.1785/gssrl.80.1.119).
- Harris, R. A., and N. A. Abrahamson (2014), Strong ground motions generated by earthquakes on creeping faults, *Geophys. Res. Lett.*, 41, 3870–3875, doi: [10.1002/2014GL060228](https://doi.org/10.1002/2014GL060228).
- Harris, R.A., M. Barall, B. Aagaard, S. Ma, D. Roten, K. Olsen, B. Duan, B. Luo, D. Liu, K. Bai, J.-P. Ampuero, Y. Kaneko, A.-A. Gabriel, K. Duru, T. Ulrich, S. Wollherr, Z. Shi, E. Dunham, S. Bydlon, Z. Zhang, X. Chen, S.N. Somala, C. Pelties, J. Tago, V.M. Cruz-Atienza, J. Kozdon, E. Daub, K. Aslam, Y. Kase, K. Withers, and L. Dalguer, (2018) A suite of exercises for verifying dynamic earthquake rupture codes, *Seismol. Res. Lett.*, 89, 1146-1162, doi:10.1785/0220170222
- Hastings, W. (1970), Monte Carlo sampling methods using Markov chains and their applications, *Biometrika*, 57, 97–109.
- Hough, S. E. and S. S. Martin (2015), The 1868 Hayward Fault, California, Earthquake: Implications for Earthquake Scaling Relations on Partially Creeping Faults. *Bull. Seismol. Soc. Am.*, 105(6), 2894–2909. doi: <https://doi.org/10.1785/0120140372>
- Kanamori, H., & Rivera, L. (2006). Energy partitioning during an earthquake. *American Geophysical Union Geophysical Monograph Series* 170. doi: 10.1029/170GM03
- Kelson, K. and J. Wesling (2014). Preliminary Observations of Surface Cracking Within the Epicentral Area of the M6.0 South Napa Earthquake of August 24, 2014, in Bray, J. et al. eds., *Geotechnical Engineering Reconnaissance of the August 24, 2014 M6 South Napa Earthquake*, Report of the NSF Sponsored GEER Association Team.
- Lapusta, N. and Y. Liu (2009) Three-dimensional boundary integral modeling of spontaneous earthquake sequences and aseismic slip, *J. Geophys. Res. Solid Earth*; Vol. 114; No. B9ISSN 0148-0227
- Lienkaemper, J. J., G. Borchardt, and M. Lisowski (1991), Historic creep rate and potential for seismic slip along the Hayward fault, California, *J. Geophys. Res. Solid Earth*, 96, 18,261–18,283.
- Lienkaemper, J. and P. Williams (2007), A Record of Large Earthquakes on the Southern Hayward Fault for the Past 1800 Years. *Bull. Seismol. Soc. of Am.*, 97, 1803-1819. doi:10.1785/0120060258.
- Lienkaemper, J. J., S. B. DeLong, C. J. Domrose, and C. M. Rosa (2016), Afterslip behavior following the 2014 M6.0 South Napa earthquake with implications for afterslip forecasting on other seismogenic faults, *Seismol. Res. Lett.*, 87, 609–619, doi:10.1785/0220150262.
- Lozos, J. C., D. D. Oglesby, B. Duan, and S. G. Wesnousky (2011), The effects of fault bends on rupture propagation: a geometrical parameter study, *Bull. Seismol. Soc. Am.*, 101(1), 385-398.
- Lozos, J. C. (2013), Dynamic rupture and ground motion modeling on realistically complex strike-slip faults, PhD dissertation, Univ. of California, Riverside.
- Lozos, J. C., R. A. Harris, J. R. Murray, and J. J. Lienkaemper (2015a), Dynamic rupture models of earthquakes on the Bartlett Springs Fault, Northern California, *Geophys. Res. Lett.*, 42, 4343–4349, doi:10.1002/2015GL063802.
- Lozos, J.C., D. D. Oglesby, J. N. Brune, K. B. Olsen (2015b) Rupture and ground-motion models on the Northern San Jacinto fault, incorporating realistic complexity *Bull. Seismol. Soc. of Am.*, 105, 1931-1946, doi:10.1785/0120140327

- McFarland, F. S., J. J. Lienkaemper, and S. J. Caskey (2016), Data from theodolite measurements of creep rates on San Francisco Bay region faults, California: 1979-2015, Open File Rep. 2009-1119, U.S. Geol. Surv., Menlo Park, Calif.
- Metropolis, N., A. Rosenbluth, M. N. Rosenbluth, A. H. Teller, and E. Teller (1953), Equations of state calculations by fast computing machines, *J. Chem. Phys.*, 21, 1087–1092.
- Johanson, I. A., E. J. Fielding, F. Rolandone, and R. Bürgmann (2006), Coseismic and postseismic slip of the 2004 Parkfield earthquake from space-geodetic data, *Bull. Seismol. Soc. Am.*, 96, S269–S282.
- Murray, J. R., and J. Langbein (2006), Slip on the San Andreas fault at Parkfield, California over two earthquake cycles and the implications for seismic hazard, *Bull. Seismol. Soc. Am.*, 96, S283—S303.
- Nadeau, R. M., and L. R. Johnson (1998), Seismological studies at Parkfield VI: Moment release rates and estimates of source parameters for small repeating earthquakes, *Bull. Seismol. Soc. Am.*, 88, 790–814.
- Oglesby, D. D. (2008), Rupture termination and jump on parallel offset faults, *Bull. Seismol. Soc. Am.*, 98(1), 440-447.
- Richards-Dinger K. and J. H. Dieterich (2012), RSQSim Earthquake Simulator. *Seismol. Res. Lett.*, 83, 983–990, doi: <https://doi.org/10.1785/0220120105>
- Ruina, A. (1983), Slip instability and state variable friction laws, *J. Geophys. Res.*, 88, 10,359–10,370.
- Ryan, K. J. and D. D. Oglesby (2014). Dynamically modeling fault stepovers using various friction laws, *J. Geophys. Res. Solid Earth*, 119, doi: 10.1002/2014JB011151
- Schmidt, D. A., R. Bürgmann, R. M. Nadeau and M. d'Alessio (2005), Distribution of aseismic slip rate on the Hayward fault inferred from seismic and geodetic data, *J. Geophys. Res.*, 110, B08406, doi: [10.1029/2004JB003397](https://doi.org/10.1029/2004JB003397)
- Thomas, A. L. (1993), POLY3D: A three-dimensional, polygonal element, displacement discontinuity boundary element computer program with applications to fractures, faults, and cavities in the Earth's crust, Master's thesis, 52 pp., Stanford Univ.
- Waldhauser, F., and D. P. Schaff (2008), Large-scale relocation of two decades of Northern California seismicity using cross-correlation and double-difference methods, *J. Geophys. Res.*, 113, B08331, doi:10.1029/2007JB005479.
- Watt, J., D. Ponce, T. Parsons and P. Hart (2016), Missing link between the Hayward and Rodgers Creek faults, *Sci. Adv.* 2, e1601441, doi:10.1126/sciadv.1601441
- Wesnousky, S. G. (2008), Displacement and Geometrical Characteristics of Earthquake Surface Ruptures: Issues and Implications for Seismic-Hazard Analysis and the Process of Earthquake Rupture. *Bull. Seismol. Soc. Am.*, 98 (4): 1609–1632. doi: <https://doi.org/10.1785/0120070111>
- Yu, E., and P. Segall (1996), Slip in the 1868 Haward earthquake from the analysis of historical triangulation data, *J. Geophys. Res.*, 101, 16,101–16,118